Entropy-Based Coherence Metric for Land Applications of GNSS-R

Ilaria Mara Russo, *Member, IEEE*, Maurizio di Bisceglie, *Member, IEEE*, Carmela Galdi, *Member, IEEE*, Marco Lavalle, *Member, IEEE*, and Cinzia Zuffada, *Senior Member, IEEE*

***Abstract*— A novel metric for detecting coherence in global navigation satellite system reflectometry (GNSS-R) signals is presented and evaluated. It applies the Von Neumann information entropy metric for density matrices, a powerful indicator of the degree of mixing between states, coherent and incoherent, of the scene under investigation. The metric is applied to a set of raw IF data acquired by the cyclone global navigation satellite system (CYGNSS) observatories over Lake Okeechobee FL, in order to test the sensitivity of the entropy to different land cover types, including wetlands and open water. Visual comparison of results with Sentinel-1 images provides a first step in the validation of the effectiveness of entropy in detecting the presence of water covered by emergent vegetation. In addition, the entropy-based metric could be implemented on future space-based GNSS-R receivers to adapt the incoherent integration times to the observed scene, thus achieving an improvement in along-track resolution.**

***Index Terms*— Bistatic scattering, coherency, cyclone global navigation satellite system (CYGNSS), eigenvalue decomposition, entropy, global navigation satellite system reflectometry (GNSS-R).**

I. Introduction

A GROWING number of Earth monitoring applications are developing around the concept of global navigation satellite system reflectometry (GNSS-R). Originally proposed for ocean altimetry [1] and successfully applied to ocean wind speed retrieval from airborne and spaceborne receiving systems [2]–[4], GNSS-R was proven to be an innovative remote sensing technique for studying land surfaces [5]–[8], showing responsiveness to a variety of geophysical parameters, such as soil moisture, ice/snow, freeze/thaw, biomass, and wetlands. Sensitivity to these variables has also been recently confirmed by several experimental campaigns from ground-based, airborne, and spaceborne platforms [9]–[16], showing that bistatic scattering from land can be dominated by a significant coherent component, depending on the electromagnetic response of the observed surface to the incoming waveform. Coherent reflections are often observed in the presence of calm waters such as rivers and lakes, even of small size (sub-kilometer) entering the GNSS-R footprint. Inundated areas under varying vegetation cover, such as wetlands, also produce specular scattering that is much stronger than the diffuse scattering from surrounding dry lands. When coherent reflection is dominant, the area of collection is approximately equal to the first Fresnel zone (FFZ), much smaller than the area of collection corresponding to diffuse scattering. Consequently, the spatial resolution is higher than the nominal 25 km along track of the ocean surface wind speed product that the most recent GNSS-R mission, CYGNSS, routinely provides [4]. The aforementioned characteristics, i.e., high power and relatively fine spatial resolution, are attractive for remote sensing and make the detection of coherent reflections in GNSS-R an essential task that is paving the way to novel applications, including global inland water mapping, floods detection, and wetlands monitoring [17]–[19]. More specifically, monitoring the dynamics and extent of wetlands, which has driven this research work, represents a challenge due to their intrinsic heterogeneity. Wetlands are complex transitional zones between upland and aquatic ecosystems and play an essential role in the global hydrological and biogeochemical cycles. Wetlands are often characterized by the presence of open water, soil, and water covered by herbaceous and woody vegetation. They are also highly dynamic, with water level and water extent that may change over short (months) to long (decades) time scales. Some wetlands are covered by water throughout the year, whereas others show the presence of water only seasonally, due to water evaporation during the dry season. Because wetlands can be found at all latitudes, from tropical to polar regions, soil and vegetation characteristics can also vary across different wetlands. Vegetation can be dominated by herbaceous plants, shrubs, or trees with varying height above the water surface, forming a rich, highly dynamic, ecosystem. Due to these characteristics, it is desirable to map location, water level, water extent, and vegetation and soil properties routinely and with high frequency. GNSS-R provides a unique opportunity to capture the dynamic of this ecosystem with high spatial and temporal sampling, even in consideration of the increasing number of GNSS platforms.

Several previous works have proposed methods for detecting the degree of coherence in reflected GNSS signals, most of

Manuscript received May 3, 2021; revised September 9, 2021; accepted October 29, 2021. Date of publication November 8, 2021; date of current version February 15, 2022. The work performed at the Jet Propulsion Laboratory was supported by the National Aeronautics and Space Administration under Contract 80NM0018D000 with Caltech. The work of Ilaria Mara Russo, Maurizio di Bisceglie, and Carmela Galdi was supported by Università degli Studi del Sannio through the University Research Funding Programme. The work of Marco Lavalle and Cinzia Zuffada was supported by NASA ROSES under Grant NNH17ZDA001N. *(Corresponding author: Ilaria Mara Russo.)*

Ilaria Mara Russo, Maurizio di Bisceglie, and Carmela Galdi are with the Department of Engineering, Università degli Studi del Sannio, 82100 Benevento, Italy (e-mail: imrusso@unisannio.it; dibisceg@unisannio.it; galdi@unisannio.it).

Marco Lavalle and Cinzia Zuffada are with the Jet Propulsion Laboratory, California Institute of Technology, Pasadena, CA 91109 USA (e-mail: marco.lavalle@jpl.nasa.gov; cinzia.zuffada@jpl.nasa.gov).

Digital Object Identifier 10.1109/TGRS.2021.3125858

which have been developed for sea ice detection and carrier-phase altimetry. It is possible to group them into two categories depending on the GNSS-R observables used. The first group includes algorithms exploiting the amplitude of delay-Doppler map (DDM). They are based either on signal-to-noise ratio (SNR) [20], [21], on trailing edge slope (TES) [13], [22], matched filter approach [13], or on the spread of power in delay and Doppler 2-D domain [13], [23], [24]. These algorithms use the Level-1 data, which contains the real-valued DDM powers recorded after noncoherent integration. The second group takes advantage of both the amplitude and phase of DDMs, obtained after coherent integration of the Raw-IF data. As a result, these algorithms are able to provide a resolution improvement in the satellite along-track direction. The detector presented in [25] is based on the normalized coherent sum of the 1-ms complex DDM peak values over a time window. Instead, Roesler *et al.* [26] calculated circular statistics i.e., circular length and circular kurtosis from variations of the specular point phase, as indicators of GNSS-R signal coherence.

In this article, a new coherence metric, falling in the second group, and built upon the previous work in [27], is introduced and evaluated. The metric exploits the concept of entropy as a measure of the amount of information contained in the eigenvalues of the correlation matrix of the complex zero-Doppler delay waveforms. Besides the application to wetlands, the idea can be applied more widely to detect signal coherence on land, ice, or water surfaces.

This article is organized as follows. Section II provides an overview of bistatic scattering over land, with its coherent and incoherent components. Section III describes the signal model and the entropy-based coherence metric. Sections IV and V provide a general description of the site selected for algorithm validation and the datasets considered in this study and results, respectively. Finally, Section VI outlines conclusions and further research perspectives.

II. GNSS-R Scattering Over Land

In contrast to ocean where bistatic reflections are mostly incoherent, the reflected GNSS signals over land surfaces comprise typically a combination of coherent and incoherent components in different proportions. Thus, as formalized in [28], the total received mean power obtained by cross-correlating the reflected signal with a replica of the transmitted signal over a range of time delays, τ, and Doppler frequencies, f, is given as

$$\left\langle |Y(\tau, f)|^2 \right\rangle = \left\langle |Y_{\text{coh}}(\tau, f)|^2 \right\rangle + \left\langle |Y_{\text{inc}}(\tau, f)|^2 \right\rangle. \quad (1)$$

The weight of each component depends on multiple factors related to the properties of the reflecting surface, including its permittivity [29], topography [30], [31], and amount and distribution of water and vegetation. While the dielectric properties have an impact on the magnitude of the reflected power, the topographic and land cover features are mainly responsible for the type of scattering that takes place on the surface, as explained further next. In addition, the configuration of the system, particularly the receiver altitude, plays a key role on the received scattering. As shown by Martin *et al.* [32] using experimental data, the ratio between coherent and incoherent components for a spaceborne GNSS-R system is lower than that from an airborne or a ground-based platform.

With regard to the coherent component, it originates from the mirror-like reflection of the signal off the Earth's surface. This specular scattering occurs on surfaces that can be considered smooth compared to the wavelength λ. A measure of the effective surface roughness is given by the Rayleigh parameter [33]

$$R_a = 2\pi \left\langle \Delta h^2 \right\rangle^{1/2} \cos\theta / \lambda \quad (2)$$

where Δh is the surface height with respect to the mean sea level and θ is the incidence angle. From (2), it follows that coherence is maintained for small-to-moderate values of the Rayleigh parameter ($R_a \leq 1$). With 1.575-GHz center frequency signals, this condition is verified for surface rms height not exceeding 3–5 cm (depending on incidence angle) [34], [35]. This requirement, over land, is mainly met by inland water bodies such as lakes, rivers, and wetlands, without significant flow. In this case, the surface roughness is primarily due to wind-driven waves. The range of wind speed values to which the coherent reflection will be sensitive depends on the characteristics of the water body itself, such as water boundary shape, depth, and fetch, as well as the reflection geometry [36]. Even bare soils, vegetated fields, and arid desert regions can produce primarily coherent returns, as long as the surface rms height satisfies the requirement $R_a \leq 1$.

Efforts are ongoing to model the coherent component of the received GNSS-R signal power [28], [37]–[40]. For a large plane surface characterized by a small-scale roughness, it can be expressed as

$$\left\langle |Y_{\text{coh}}(\tau, f)|^2 \right\rangle = \frac{P_t G_t}{4\pi (R_t + R_r)^2} \frac{\lambda^2 G_r}{4\pi} |\chi(\tau, f)|^2 \gamma \, |\Gamma|^2 \psi \quad (3)$$

where $P_t G_t$ is the equivalent isotropically radiated power (EIRP) of the transmitted signal, G_r is the receiver antenna gain, R_t and R_r are the distance from transmitter and receiver to the specular point, respectively, and χ is the Woodward ambiguity function (WAF). From (3), it is also understood that the received power is proportional to three parameters associated with the properties of the scattering surface: the attenuation factor γ due to vegetation absorption and volume scattering ($\gamma = 1$ in the absence of vegetation), the Fresnel reflection coefficient $|\Gamma|^2$ of the mean surface, and the decorrelation factor $\psi = \mathrm{e}^{-4R_a^2}$ due to surface roughness that depends on the Rayleigh parameter. However, this equation does not apply to coherent scattering from heterogeneous scenes with both land and water around the specular point, such as wetlands, or from surfaces that are nonhomogeneous in terms of roughness, such as inland water bodies that generally have different areas with different values of R_a. In order to capture the variability of the surface properties, a surface integral can be introduced that accounts for the different contributions across a small reflecting

surface S around the specular point [38]. This gives

$$\left\langle |Y_{\text{coh}}(\tau, f)|^2 \right\rangle = \frac{G_r G_t P_t}{(4\pi)^3} \left| \iint_S \frac{jk\sqrt{\gamma\,\psi}\cos(\theta)\Gamma(\theta)\chi(f,\tau)}{R_1 R_2} e^{-jk(R_1+R_2)} dS \right|^2. \quad (4)$$

For small values of R_a, the surface behaves like a specular reflector, only slightly degrading the coherence of the reflected signal. Still, theoretical models predict the presence of a weak incoherent component [41]. As the surface roughness increases ($R_a > 1$), the coherent component of the reflected GNSS signal quickly vanishes, whereas the incoherent component becomes progressively stronger, such as on rough or densely vegetated surfaces. These incoherent returns are produced by diffuse scattering mechanisms that take place due to the random structure of the terrain surface and volume scattering [42], [43]. In this case, the power is modeled by the bistatic radar equation [44]

$$\left\langle |Y_{\text{inc}}(\tau, f)|^2 \right\rangle = \frac{\lambda^2 P_t}{(4\pi)^3} \iint \frac{G_t G_r |\chi(\tau, f)|^2}{R_1^2 R_2^2} \gamma\,\sigma^0 dS \quad (5)$$

where R_1 and R_2 are the ranges from the transmitter and the receiver to the point on the surface, respectively, γ is a vegetation attenuation parameter, and σ^0 is the surface normalized bistatic radar cross section (NBRCS).

The predominance of one component over another has an effect on the achievable spatial resolution, an aspect of considerable importance for remote sensing applications. In a coherent scattering regime, the returns are confined to the specular point and a small region around it, to first order taken to be the FFZ [40] with dimensions dependent on the observation geometry. Typically, the FFZ is smaller than 1 km from an low Earth orbit (LEO) satellite. Strictly speaking, the accurate quantification of the spatial extension of the contributing region for inhomogeneous scenes in coherent reflection regime is still under discussion, as pointed out in recent studies [38], [45], [46]. Coherent scattering results in a DDM characterized by a strong peak power in the delay-Doppler bin corresponding to the position of the specular point and a concentration of power in a few bins around the peak. In this case, in fact, the reflected waveform has the shape of the GNSS signal ambiguity function. However, for inhomogeneous scenes, the peak power fluctuates with characteristics of the contributing Fresnel zones. By contrast, in incoherent scattering regime, the size of the scattering area extends further away from the first few Fresnel zones, increasing along with the surface roughness. This translates into a DDM where the power is spread over many more delay-Doppler bins and the reflected waveform is wider and weaker than the coherent one.

III. Coherence Metric

The received GNSS-R signal is usually given as a superposition of replicas of the scattered signal in the continuum [28]. This model will be adopted in Section III-A to obtain a discrete vector representation of the received waveform where both coherent scattering and incoherent scattering are included as in (1) for powers. Given the received signal model, a metric for determining the level of signal coherence is derived in the following. The idea relies on the generalized eigendecomposition (GED) of the complex correlation matrix of the received signal (Section III-B) and exploits the concept of information entropy, derived in Section III-C.

A. Received Signal Model

The GPS transmitted C/A signal $s(t)$ is given as [47]

$$s(t) = c(t)e^{j(2\pi f_0 t + \phi)} \quad (6)$$

where f_0 is the carrier frequency, ϕ is the carrier phase, and $c(t)$ is the C/A code with the embedded navigation signal. The received signal $y(t)$ is the sum of a coherent component, an incoherent component $y_{\text{inc}}(t)$, and the thermal noise $n(t)$, which is usually modeled as a white Gaussian random process. The coherent component in [38] can be approximated by a finite number of returns from surface patches, and therefore,

$$y(t) = \sum_{n=1}^{D} A_n s(t - t_n) e^{j2\pi f_n t} + y_{\text{inc}}(t) + n(t) \quad (7)$$

where D is the number of scattered components of the coherent contribution, each having an amplitude A_n, a delay t_n, and a frequency shift f_n. The amplitude of the received coherent returns from each surface patch of area δS, omitting for ease of notation the dependence of all terms by the patch index, is

$$A = \frac{jkE_0\sqrt{\gamma\,\psi}\cos(\theta)\Gamma(\theta)\delta S}{4\pi R_t R_r} e^{-jk(R_t+R_r)} \quad (8)$$

where E_0 denotes the amplitude of the transmitted field. Note that, if the surface is homogeneous and flat, the power of the coherent component is given in (3).

At the receiving front end, the signal is downconverted and correlated with a local replica of the transmitted pseudorandom noise (PRN) code sequence, over a time interval T, for different Doppler frequency values. This operation leads to the generation of the delay-Doppler map

$$Y(\tau, f) = \sum_{n=1}^{D} A_n e^{-j2\pi f_0 t_n} \chi_c(\tau - t_n, f - f_n) + Y_{\text{inc}}(\tau, f) + N(\tau, f) \quad (9)$$

where $\chi_c(\cdot,\cdot)$ is the ambiguity function of the transmitted PRN sequence, $Y_{\text{inc}}(\cdot,\cdot)$ is the incoherent component of the delay-Doppler map, and $N(\cdot,\cdot)$ is the cross correlation between the Doppler-shifted PRN sequence and the noise process. Therefore, the additive noise is colored with correlation length τ_c, that is, the chip duration of the PRN sequence. The zero-Doppler complex delay profile, in the variable τ, can be expressed as

$$z(\tau) = \sum_{n=1}^{D} A_n e^{-j2\pi f_0 t_n} r_c(\tau - t_n, -f_n) + y_{\text{inc}}(\tau) + n(\tau) \quad (10)$$

where $r_c(\tau, f_n)$ denotes the f_n Doppler frequency cut of the WAF, which is given by

$$r_c(\tau, f_n) = \frac{1}{T} \int_0^T c(t)c(t+\tau)e^{-j2\pi f_n t} dt \quad (11)$$

that is approximately a triangular function in the variable τ with delay spread $\pm\tau_c$ around the correlation peak. In (10), $y_{\text{inc}}(\tau)$ is the zero Doppler complex delay profile of the incoherent component and $n(\tau) = N(\tau, 0)$.

The delay profile signal is sampled at M equispaced lags to obtain a delay profile vector $\mathbf{z} = \mathbf{z}(iT_s) = [z(\tau_1), z(\tau_2), \ldots, z(\tau_M)]^T$. It is assumed that the sampling period T_s is chosen to be a small fraction of the chip duration. This ensures that the overall number of delay samples M is greater than the number D of components of the coherent contribution, a condition that will be clarified later. From (10), the vector $\mathbf{z}$ can be expressed as

$$\mathbf{z} = \sum_{n=1}^{D} A_n e^{-j2\pi f_0 t_n} \mathbf{r}_c(t_n, -f_n) + \boldsymbol{\nu} \tag{12}$$

where $\mathbf{r}_c(t_n, -f_n) = [r_c(\tau_1 - t_n, -f_n), r_c(\tau_2 - t_n, -f_n), \ldots, r_c(\tau_M - t_n, -f_n)]^T$ is the "steering vector" or mode vector and $\boldsymbol{\nu}$ is the sum of the incoherent contribution vector $\mathbf{y}_{\text{inc}} = [y_{\text{inc}}(\tau_1), y_{\text{inc}}(\tau_2), \ldots, y_{\text{inc}}(\tau_M)]^T$ and the noise vector $\mathbf{n} = [n(\tau_1), n(\tau_2), \ldots, n(\tau_M)]^T$. Denoting also as $\boldsymbol{\Gamma} = [\mathbf{r}_c(t_1, -f_1), \mathbf{r}_c(t_2, -f_2), \ldots, \mathbf{r}_c(t_D, -f_D)]$ the $(M \times D)$ steering vectors matrix and $\mathbf{g} = [A_1 e^{-j2\pi f_0 t_1}, A_2 e^{-j2\pi f_0 t_2}, \ldots, A_D e^{-j2\pi f_0 t_D}]^T$ the path-gain vector, the delay profile can be finally written in the vector form

$$\mathbf{z} = \boldsymbol{\Gamma}\mathbf{g} + \boldsymbol{\nu}. \tag{13}$$

From a geometric point of view, the data vector $\mathbf{z}$ can be visualized as a vector in the M dimensional space. In the absence of noise and incoherent contribution, it is confined to the signal subspace whose dimension is not greater than the number D of signal components. Therefore, the condition $M > D$ ensures that a subspace of dimension $M - D$ contains only the incoherent and noise contributions. This property will be exploited in Section III-B where the eigendecomposition of the data vector correlation matrix is used to investigate the dimensionality of the signal subspace or, in other words, the number of coherent components.

B. Signal Eigendecomposition

The linear form in (13) has gained great interest in the context of multiple signal classification (MUSIC) where the problem is to determine the parameters of a combination of waveforms received by an array of sensors [48]–[50]. Applications include estimation of the number of signals and direction of arrival in communication theory and target tracking in radar systems. Indeed, in GNSS reflectometry, a number of coherently reflected waveforms with different amplitudes, delays, and phases are sensed from several positions of the receiving platform, which generates a synthetic array of sensors. With reference to the model derived in Section III-A, this section provides the basic framework for application of the signal decomposition to the problem of finding a signal coherence metric. Thus, from (13), the correlation matrix of the vector $\mathbf{z}$ can be calculated as

$$\mathbf{R} = \boldsymbol{\Gamma}\boldsymbol{G}\boldsymbol{\Gamma}^H + \mathbf{R}_\nu \tag{14}$$

where the notation $(\cdot)^H$ indicates the Hermitian operator, $\boldsymbol{G} = E[\mathbf{g}\mathbf{g}^H]$ is the path-gain correlation matrix, and $\mathbf{R}_\nu$ can be expressed as

$$\mathbf{R}_\nu = E\left[\boldsymbol{\nu}\boldsymbol{\nu}^H\right] = \sigma^2 \mathbf{R}_c + \mathbf{R}_y^{\text{inc}}. \tag{15}$$

Note also that $\mathbf{R}_c$ is a Toeplitz matrix whose klth element is the autocorrelation function of the PRN sequence at lag $k - l$ and $\mathbf{R}_y^{\text{inc}}$ is the autocorrelation function of the incoherent component, where it is also assumed that the mutual correlation between the noise and the incoherent component is identically zero.

The GED

$$\mathbf{R}\boldsymbol{e}_i = \lambda_i \mathbf{R}_\nu \boldsymbol{e}_i, \quad i = 1, 2, \ldots, M \tag{16}$$

performs a simultaneous diagonalization of $\mathbf{R}$ and $\mathbf{R}_\nu$. Denoting by $\boldsymbol{\Phi}$ the eigenvectors matrix and by $\boldsymbol{\Lambda}$ the eigenvalues matrix, (16) can be written as

$$\mathbf{R}\boldsymbol{\Phi} = \mathbf{R}_\nu \boldsymbol{\Phi}\boldsymbol{\Lambda} \tag{17}$$

that fulfills

$$\begin{cases} \boldsymbol{\Phi}^T \mathbf{R} \boldsymbol{\Phi} = \boldsymbol{\Lambda} \\ \boldsymbol{\Phi}^T \mathbf{R}_\nu \boldsymbol{\Phi} = \mathbf{I}. \end{cases} \tag{18}$$

Equation (16) requires three conditions to be met. First, the columns of $\boldsymbol{\Gamma}$ are linearly independent. Second, $\boldsymbol{G}$ is not singular. Third, the number of samples of the delay profile vector is greater than D $(M > D)$ [48], [49].

Several observations are useful:

1) The matrix $\mathbf{R}$ is not known. It can be estimated from N sequential snapshots of the delay profile vector as

$$\widehat{\mathbf{R}} = \frac{1}{N}\mathbf{Z}\mathbf{Z}^H \tag{19}$$

where $\mathbf{Z}$ is the $M \times N$ matrix whose columns are the N sequential snapshots of the delay profile vector $\mathbf{z}(n)$.

2) The matrix $\mathbf{R}_\nu$ is known as regards the thermal noise component $\mathbf{R}_c$, whereas the incoherent component is unknown nor can it be estimated from data. In the applications, only correlation of the thermal noise will be considered. A study on correlation in sea surface reflections can be found in [51] where the authors show that the correlation matrix of the incoherently scattered component extends around the main diagonal for positive values of the delay. Neglecting such component is expected to unfavorably affect the overall performance of the decomposition when the power of coherent and incoherent components is comparable.

In the following, the delay profile vector will also be referred to as waveform. It is worth noting that even if the estimation of the autocorrelation matrix requires a sequence of waveforms, the subspace analysis depends mainly on the intrawaveform correlation and not on the correlation among the different waveforms. The optimal choice of N and M parameters will be explained in Section IV-D.

C. Entropy of Eigenvalues

The Von Neumann entropy was introduced in quantum mechanics as a measure of information in a system described by the density matrix S [52]. Its definition is commonly given as

$$H = -\mathrm{Tr}(S \log S) \tag{20}$$

where S is a symmetric $k \times k$ positive semidefinite matrix, whose trace is 1. The Von Neumann entropy is equal to the Shannon entropy of a random variable whose probability distribution is given by the normalized eigenvalues. Some properties of the Von Neumann entropy are useful for the following discussion.

1) Nonnegativity: The Von Neumann entropy is nonnegative and bounded between 0 and $\log k$, where k is the matrix dimension. By choosing a base-k logarithm in (20), the entropy is bounded in $(0, 1)$.

2) Minimum Value: The minimum value of the Von Neumann entropy is obtained when the system is in a pure state, corresponding to a density matrix that is a rank one projector. This is true if only one eigenvalue of the density matrix is different from zero.

3) Maximum Value: The maximum value of the Von Neumann entropy corresponds to maximally mixed states. It is obtained when all eigenvalues are equal.

The meaning and properties of entropy suggest to use it as a valid indicator for the presence of coherent components, that is, a signal subspace well separated from the subspace corresponding to incoherent scattering and noise. The case of only one, strong coherent component can be perfectly associated with a pure state, whereas the absence of coherent components corresponds to maximally mixed states that well model a signal dominated by incoherent scattering. The Von Neumann entropy will be calculated after the GED that transforms the correlation matrix $\mathbf{R}$ into a diagonal matrix, is performed. A normalization is also needed to get a density matrix. The proper normalization factor is given by the sum of the eigenvalues, which is the trace of the diagonal matrix. Therefore, the proposed coherence metric is the entropy of the matrix

$$S = \frac{\mathbf{\Phi}^T \mathbf{R} \mathbf{\Phi}}{\mathrm{Tr}\left(\mathbf{\Phi}^T \mathbf{R} \mathbf{\Phi}\right)}. \tag{21}$$

First, it should be noted that in the presence of noise, the condition of pure state, corresponding to a rank-one density matrix, cannot be strictly achieved. However, if a strong coherent component is present, the signal subspace is very well separated from the noise subspace, the first eigenvalue is much higher than the others, and the entropy is very close to zero. A second comment is about a particular confounding condition that could arise due to the estimation of the correlation matrix, as assumed by (19). Since the pure state corresponds to a rank-one density matrix, it could be obtained, in absence of noise, in the case that all snapshots are the same, whatever the nature of coherence is. Fortunately, this situation is only ideal because the coefficients in the path-gain vector $\mathbf{g}$ are well modeled as random variables and the path-gain correlation matrix $\boldsymbol{G}$ cannot be rank-one, even when estimated from data. In the experimental analysis presented in the following, the Von Neumann entropy will be used to assess the degree of coherence of the scattered signal under different conditions related to the presence of water and to its state.

IV. Experimental Setup

A. Study Area

Lake Okeechobee was chosen as test site to illustrate and validate the entropy-based coherence metric. The lake extends for 1800 km^2 on the south-central portion of the Florida peninsula at latitudes 27°12′N–26°40′N and longitudes 81°07′W–80°37′W, as shown in Fig. 1(a). This lake is very shallow (mean depth ∼3 m) with respect to its size, with water depths varying as a function of rainfall, flood control discharges, and water supply deliveries. As shown in Fig. 1(b), Lake Okeechobee is a heterogeneous ecosystem, made up of three distinct ecological zones: 1) a littoral zone comprised of a 400-km^2 mixed marsh community of submerged aquatic vegetation and emergent vegetation along the west and south shoreline; 2) a 200-km^2 shallower near-shore zone (0.5–2 m deep) underlain by sand and peat sediments with varying water quality and coverage of submerged aquatic vegetation; and 3) a 1200-km^2 central pelagic zone with nutrient-rich turbid water, too deep (3–5 m) to support any plants.

B. CYGNSS Data

CYGNSS is a constellation of eight small satellites, launched into LEO in December 2016. Each spacecraft has a GNSS-R payload on board capable of receiving four simultaneous reflections, within a latitudinal range of approximately ±38°, so the full constellation can make up to 32 measurements simultaneously [16], [54]. Apart from DDMs and the bistatic radar cross sections, which are the main data products of this mission, the CYGNSS receivers can also be initiated by ground commands to record Raw-IF GNSS signal samples from the zenith-pointing antenna and the two starboard and port antennas for a short time period (∼60 s). Raw-IF data are recorded with 3.8724-MHz center frequency and 16.0362-MHz sampling rate and quantized as 2-bit samples. Raw-IF CYGNSS data are recorded as a bytes stream that incorporates bit pairs from zenith, starboard, and port antennas. A customized Raw-IF processor has been developed by the authors for achieving controlled signal quality, high temporal resolution, and phase coherency. Recorded data must be synchronized with the Level-1 corresponding product to recover the ancillary information that is recorded as metadata. Orbital positions and velocities of satellites are interpolated with millisecond accuracy and the specular point is estimated using corrections for mean sea level and terrain elevation. The processor makes use of the Zenith channel to acquire precise carrier frequency and code delay that are used for accurate calculation of the specular point delay. The complex autocorrelation calculated from the nadir antenna signal is produced for each millisecond. The small residual delay that is possibly accumulated during the orbital track is estimated and corrected to produce a well-aligned array of zero-Doppler waveforms. CYGNSS data products are available to the public at the

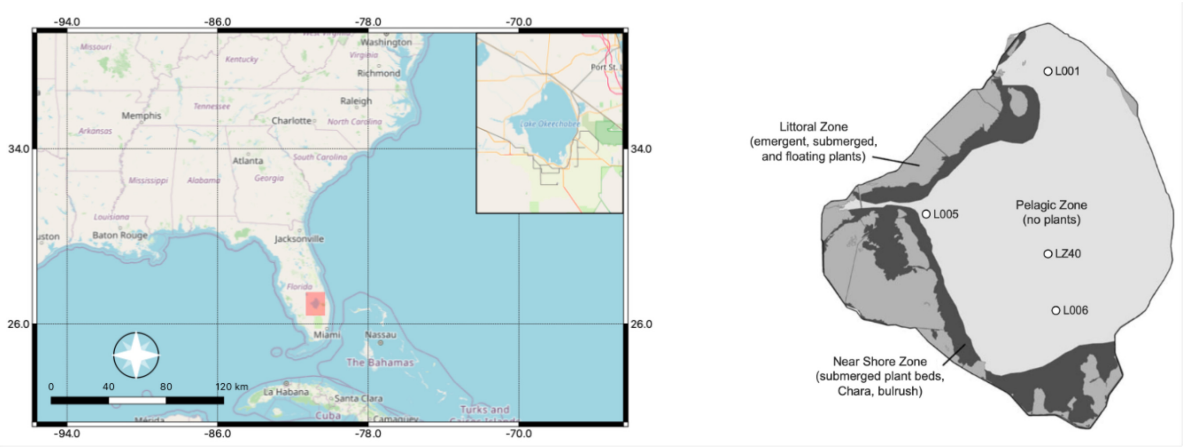

(a) (b)

Fig. 1. (a) Overview of the study area. (b) Map of Lake Okeechobee showing its major ecological zones: littoral zone, near-shore zone, and pelagic zone [53]. L001, L005, L006, and LZ40 are the weather stations managed by SFWMD.

NASA Physical Oceanography Distributed Active Archive Center (PO.DAAC; https://podaac.jpl.nasa.gov/CYGNSS).

The analysis was carried out using five CYGNSS Raw-IF tracks acquired in March and June 2020 over Lake Okeechobee, in order to explore the sensitivity of the entropy to adjacent land wetlands and different states of open water.

C. Validation Data

Several types of data have been used to support the evaluation of the coherence metric. Two ascending VV/VH Sentinel-1 (S-1) synthetic aperture radar (SAR) data have been examined in two dates closest in time to the CYGNSS tracks, i.e., February 27, 2020 and June 2, 2020. The local time of the ascending S-1 acquisitions is 6 A.M. In general, for a polarimetric SAR, four scattering mechanisms can occur on wetlands. Calm flat water leads to specular reflection, which results in low backscatter close to the radar noise floor. Rough surfaces, such as soil or water rippled by wind, produce single-bounce scattering. Vegetation typically gives rise to diffuse scattering and attenuates the microwave depending on vegetation height, structure, and dielectric constant. The presence of a flat surface covered by vegetation, especially vertical stems, can lead to double-bounce scattering return, which has typically larger intensity than the other scattering types. All four scattering types can dominate or can be mixed within the radar resolution cell depending on surface and vegetation characteristics, incident angle, radar frequency, bandwidth, and polarization. High-frequency microwaves (X- or C-band) tend to penetrate through close canopy by only a few centimeters and are sensitive to small-scale roughness; low-frequency microwaves (L- or P-band) penetrate deeper in the vegetation and tend to produce more double-bounce scattering. Full-polarimetric radars enable a better separation of the scattering mechanisms, unlike dual-polarimetric SARs, such as Sentinel-1, which offer a limited interpretation of the scattering process. In typical grayscale SAR backscatter images, wetlands appear dark over calm open water and brighter over vegetation and rough surfaces. Vegetation scattering can appear more speckly than surface scattering and it is typically relatively brighter in the HV polarimetric channel compared with the HH or VV polarimetric channels. A composite of RGB colors for each Sentinel-1 image was made using the VV channel for red, VH channel for green, and the ratio |VV|/|VH| for blue in order to facilitate the visual interpretation of the land cover in the study area. It can be observed that water and flat bare soil appear with various shades of blue, while vegetated areas appear as yellow/green. In contrast, the light purple/pink/red colors denote the presence of inundated vegetation.

Two different maps have been considered to account for the specific vegetation cover within the western marsh portion of Lake Okeechobee. The first map is provided by the South Florida Water Management District (SFWMD) and, through polygon feature classes, defines the extent and type of littoral vegetation for 2016, as shown in Fig. 2(a). Unfortunately, no such maps are available for 2020 when the CYGNSS tracks analyzed in this article were acquired. The second map, produced by the U.S. Fish and Wildlife Service and made available via the wetlands mapper [55], depicts the type and extent of wetlands for 2020 as defined in [56] [Fig. 2(b)].

Finally, wind data have been obtained from the SFWMD's DBHYDRO database (https://www.sfwmd.gov/science-data/dbhydro). SFWMD operates weather stations on Lake Okeechobee at the locations shown in Fig. 1 (L001, L005, L006, and LZ40). These data include daily mean and instantaneous measurements (at 15-min intervals). Table I shows the speed and direction of wind for each acquired CYGNSS track.

D. Parameters Setting

The estimation of the autocorrelation matrix requires N sequential delay profiles of length M. The choice of N and M has a significant impact on the performance of the entropy-based coherence metric.

TABLE I

WIND VALUES ACQUIRED FROM SFWMD WEATHER STATIONS FOR THE FIVE TRACKS ANALYZED. TWO VALUES ARE REPORTED FOR EACH TRACK: WNVS, WHICH IS THE VECTOR WIND SPEED IN m/s, AND WNVD, WHICH IS THE VECTOR WIND DIRECTION IN DEGREES CLOCKWISE FROM NORTH. INSTANTANEOUS MEASUREMENTS CLOSEST TO THE CYGNSS ACQUISITION TIME HAVE BEEN CONSIDERED

	L001	**L005**	**L006**	**LZ40**	
2020-02-22	11.98	11.17	14.01	13.59	**WNVS**
	358.1	357.9	347.5	6.5	**WNVD**
2020-02-29	8.53	5.52	10.75	10.83	**WNVS**
	325.9	315	307.8	327.6	**WNVD**
2020-06-04	1.89	1.60	2.81	3.42	**WNVS**
	132	158.4	122.5	151.9	**WNVD**
2020-06-07 (1)	5.40	5.70	5.10	5.28	**WNVS**
	147.9	145.9	118.1	136.4	**WNVD**
2020-06-07 (2)	2.69	2.45	2.34	2.14	**WNVS**
	NaN	192.7	166.6	177.1	**WNVD**

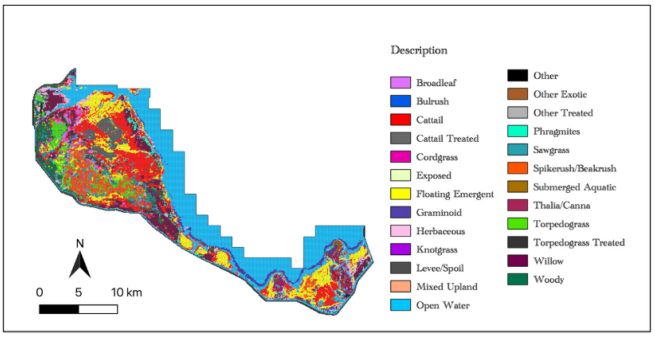

(a)

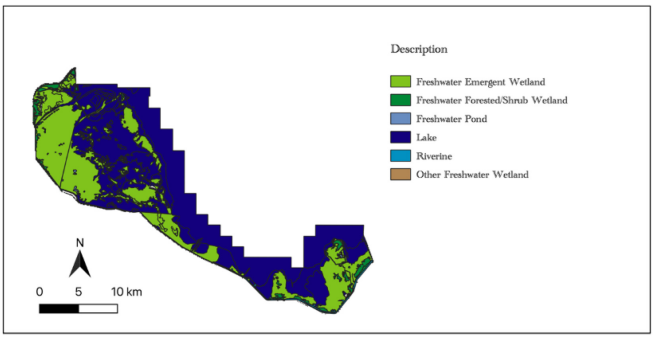

(b)

Fig. 2. Land cover classification in the southwest region of Lake Okeechobee. (a) Map of the types of vegetation for 2016, as reported by SFWMD. (b) Map of the types of wetland for 2020, available via wetlands mapper.

Regarding the number M of samples of each delay profile, it must be considered that the width of the theoretical delay profile is $2\tau_c \simeq 2 \cdot 10^{-6}$ s, being defined by the WAF. Since the sampling rate of CYGNSS Raw-IF data is 16.0362-MHz, the smallest window length required to capture the peak must be 32 samples. Nevertheless, two further aspects have to be taken into consideration: a possible window misalignment with respect to the specular point and the waveform broadening due to diffuse scattering. This leads to an increase in the size of the window. It should be noted that by enlarging the window, there is the possibility of including samples that contain thermal noise only in the estimation of the correlation matrix, whose effect is to increase entropy. A good tradeoff is represented by 48 samples, a value obtained by increasing 32 by 25% each side.

As concerns the number of delay waveforms, N has a significant impact on the spatial resolution. Since the waveforms used to estimate the single autocorrelation matrix are observations related to different specular points as the receiver moves, each entropy value will be representative of an elongated footprint along track. As a result, the higher is N, the higher is the probability that within the observed area, the heterogeneity of the targets increases with consequent inability of the algorithm to differentiate. This translates into degradation of spatial resolution. In light of these considerations, each autocorrelation matrix has been estimated from $N = 16$ waveforms, to which corresponds a resolution along the track of about 700 m (depending on how large the FFZ is).

V. RESULTS

Two major land cover types can be identified in the area of Lake Okeechobee. The first land cover is open water and will be used hereafter to test the sensitivity of the entropy-based metric to surface roughness generated by the wind. The second type of land cover is wetland and will be used to test the sensitivity of the entropy-based metric to different vegetation types and water beneath vegetation.

A. Sensitivity of Entropy to Open Water Roughness

Results of entropy calculated from tracks acquired under different wind conditions are discussed hereafter. As explained in Section II, the wave coherence is mainly determined by the small-scale surface roughness that, for inland water bodies, is mainly due to wind-driven surface waves. As the wind speed and fetch increase, the height of the waves and their peak wavelength will also increase. This effect for the lakes was thoroughly investigated in [36].

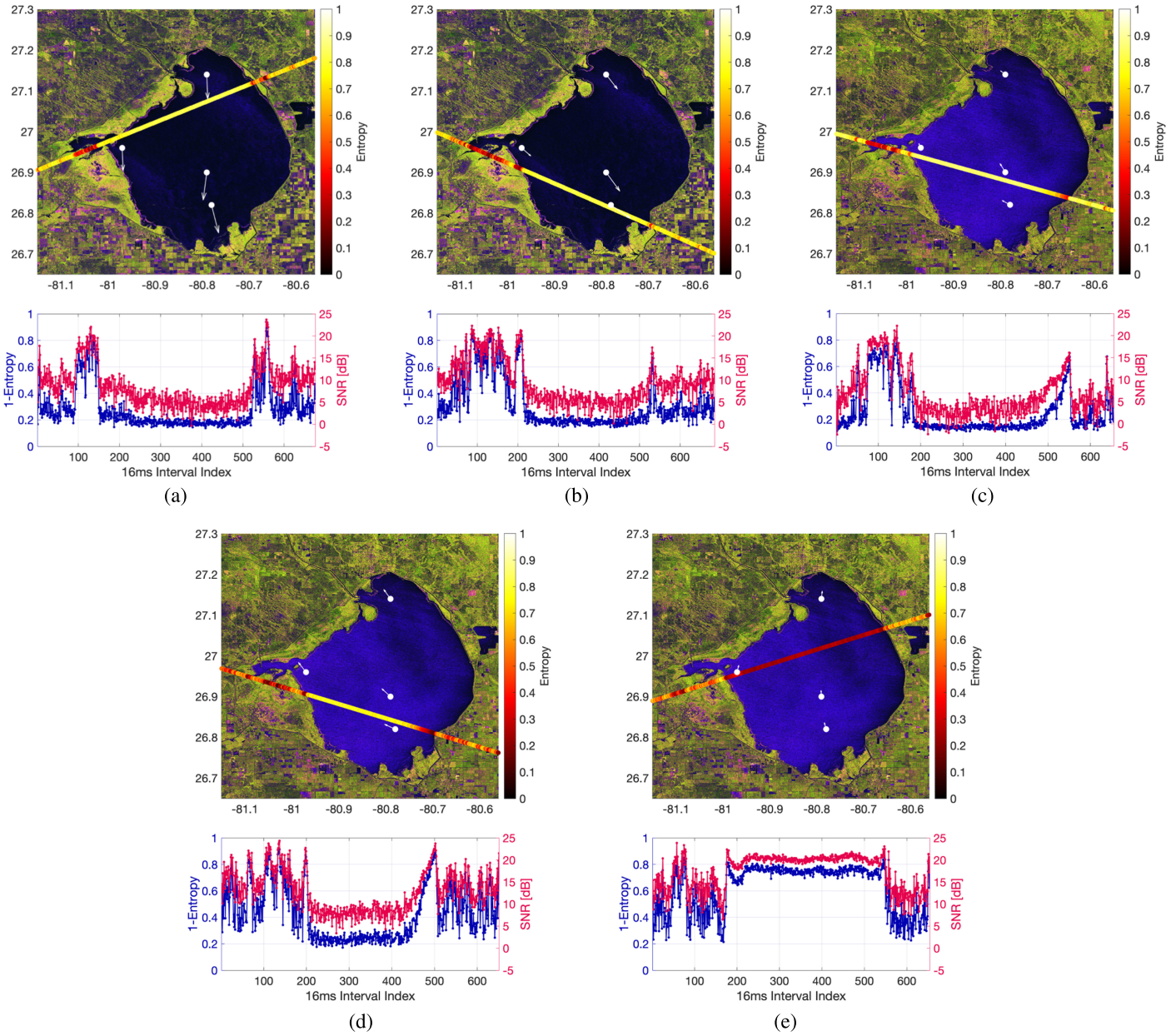

Fig. 3. Entropy results calculated on five tracks acquired on (a) February 22, 2020, (b) February 29, 2020, (c) June 4, 2020, (d) June 7, 2020 (1), and (e) June 7, 2020 (2). For each track, the entropy is superimposed on the temporally closest Sentinel-1 false-color composite. White dots represent weather stations operated by SFWMD. The arrows show the wind direction and their length is proportional to the wind speed, according to Table I. Also, for each track, the peak SNR and 1-entropy are shown in the second plot.

Fig. 3(a) and (b) shows the entropy values calculated from acquisitions on Lake Okeechobee in high wind conditions, which cause significant wave heights favored by the large size of the lake itself. As expected, the entropy is close to 1 ($\simeq$0.8) on the whole pelagic zone, which provides evidence for a strongly incoherent reflection. The crossing of the lake shoreline for both tracks is clearly visible by the abrupt jump of entropy from 0.8 to 0.2. This strong coherence detected in the area near the lake shore can be attributed to shallow water or to short enough fetch that limits the waves' height.

A similar behavior is also observed for moderate wind speed [see Fig. 3(c) and (d)]. Incoherent returns are detected on open water, with entropy values comparable to those observed in case of high wind speed. In contrast to the west shore, entropy gradually decreases near the east shore of the lake. This change indicates various levels of roughness that could be related to the value of fetch, which, in turn, depends on the wind direction, as evidenced by the simulations in [36].

Finally, Fig. 3(e) shows the entropy in low wind conditions. The calm waters of the lake generate the coherent scattering that is captured by entropy that takes very low values ($\simeq$0.2). The beginning and the end of the pelagic zone are indicated by the two lower peaks at these points.

The peak SNR for each track has also been reported in Fig. 3. Peak SNR is here defined as the ratio of the signal

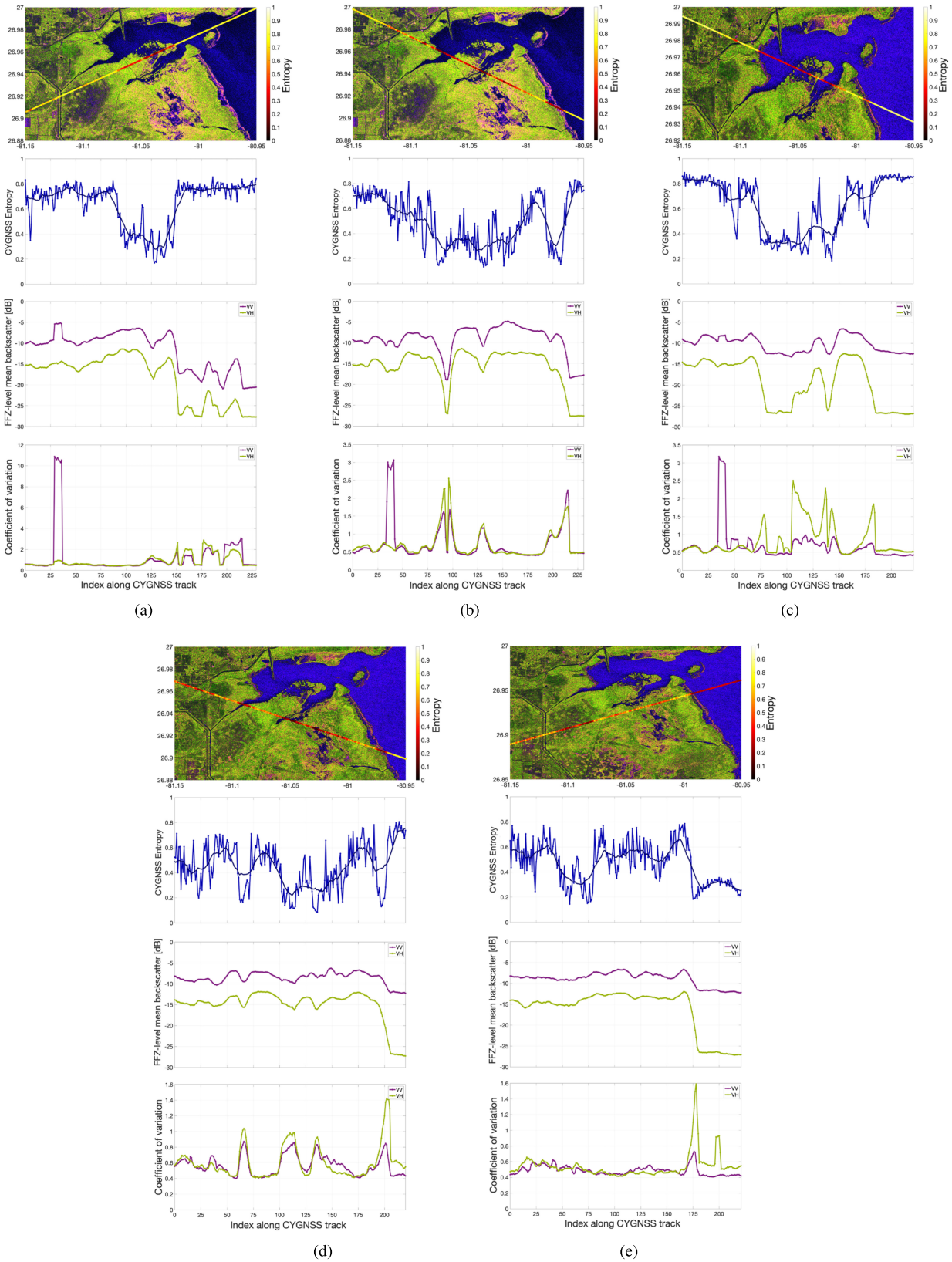

Fig. 4. Zoom over the marshy west region of Lake Okeechobee shown in Fig. 3 for the CYGNSS tracks acquired on (a) February 22, 2020, (b) February 29, 2020, (c) June 4, 2020, (d) June 7, 2020 (1), and (e) June 7, 2020 (2). Three plots are also provided for each track: the first plot shows the CYGNSS entropy, the second plot displays Sentinel-1 backscatter values along transects corresponding to CYGNSS tracks and averaged within the FFZ, and the third plot reports the coefficient of variation calculated for each FFZ.

power minus the noise power to the noise power. Signal power was estimated at the specular point, whereas noise power was computed by averaging a subset of samples of the zero-Doppler delay waveform where the signal was absent,

i.e., located at negative delays, sufficiently far from the specular point. As shown in Fig. 3, peak SNR plots show high correlation with $1 - H$. This is due to the reflected power in the forward scattering from rough surfaces; in the presence of larger roughness, both signal coherence and scattered power in the specular direction reduce. However, SNR curves reveal greater variance than entropy and some difficulty in identifying regions where partially coherent scattering occurs. Thus, an advantage of using the entropy metric is that the scattered waveform is accounted more extensively in its shape, in contrast to the peak SNR that only accounts for a single value. In addition, unlike SNR, entropy has a fixed dynamic range between 0 and 1, allowing for straightforward comparison of coherence detection in a wide range of situations and for a variety of targets. Automatic detection of dominantly coherent and incoherent returns could be implemented by setting a fixed threshold value between 0 and 1 on the estimated entropy.

B. Sensitivity of Entropy to Wetland Type

The marshy west region of Lake Okeechobee, as shown in the most recent map available in Fig. 2(a), is a mosaic of diverse vegetation types, including spikerush (*Eleocharis cellulosa*), cattail (*Typha*), willow (*Salix caroliniana*), torpedograss (*Panicum repens*), and smartweed (*Polygonum hydropiperoides*). The spatial distribution and composition of plant communities undergo year-to-year variation, primarily as a function of water level change. For example, over the past years, the spatial extent of willow has declined, while the cattail has expanded to surround spikerush sloughs in the interior littoral zone [57].

In order to corroborate the entropy-based metric on this marshy area, backscatter values of Sentinel-1 along transects corresponding to CYGNSS tracks are also provided in Fig. 4. More specifically, for each entropy value, the mean of the S-1 pixels falling within the corresponding FFZ was calculated. Furthermore, to account for scene heterogeneity inside the FFZ, the coefficient of variation, defined as the ratio of standard deviation to the mean of the pixels, was computed. Focusing on the left portion of the CYGNSS track in Fig. 4(a), the entropy shows a sharp transition from high (>0.5) to low values (<0.4). From the comparison with the land cover classification maps in Fig. 2, samples with high entropy are characterized by freshwater emergent wetland as shown in Fig. 2(b), whereas samples with low entropy are marked by floating/emerging vegetation shown in Fig. 2(a) and by the lake delineated in Fig. 2(b). Therefore, the lower values of entropy correctly indicate the presence of water even when the surface is covered by floating vegetation. Higher values of entropy characterize instead the area of emergent vegetation that is generally a shore zone and only temporarily flooded [56]. It is interesting to note that the distinction between the two vegetation types is not visible from the Sentinel-1 VH/VV composite, most likely due to limited penetration of the C-band microwaves into vegetation and inability to discriminate among different vegetation types. Note also that entropy values drop further to below 0.2–0.3 over samples with low Sentinel-1 backscatter due to more coherent reflection caused by the larger fraction of calm water nonobstructed by vegetation within the CYGNSS footprint. Continuing toward the right portion of the CYGNSS track, entropy becomes high again, with values ranging between 0.75 and 0.9. This segment starts where Sentinel-1 data show a clear reduction in VH/VV composite backscatter due to the presence of open water. However, the presence of peaks in the backscatter curves at the index 150–225 is attributable to averaging within the FFZ, which encompasses areas with different cover types (lake and land) as confirmed by the coefficient of variation. Interestingly, entropy values over open water tend to be correlated with the "openness" of the water, as observed from Fig. 4(b) and (c). In Fig. 4(b) and (c), the right portion of the CYGNSS track falls on the open lake (cf. with Fig. 3) where the effects of the wind are more prominent compared to areas of open water surrounded by land, such as those toward the middle and the left portion of the track where entropy appears significantly lower. For water covered by vegetation, entropy is consistently high near the coast in Fig. 4(b)–(d) where Sentinel-1 samples are light green [$-81°$ longitude and 26.95° latitude in Fig. 4(c)]. These samples have higher VH backscatter and, therefore, denser or taller vegetation compared to the surrounding area, which causes more absorption and a weaker, less coherent reflection of the CYGNSS signal leading to higher entropy. Fig. 2(a) reports willow/phragmites as dominant vegetation type in this area also confirmed by the wetland classification in Fig. 2(b), showing the presence of freshwater emergent wetland. Another interesting feature of the entropy over wetlands is the inverse correlation with the SAR double-bounce backscatter that appears as purple samples in the Sentinel-1 images of Fig. 4. These samples are visible as a cluster near the coast and also interspersed with the green vegetated samples. Entropy tends to be lower over Sentinel-1 purple pixels due to the less dense vegetation or larger presence of water under vegetation, both having the effect of increasing the double-bounce backscatter (VV polarimetric channel) and the coherency of the CYGNSS signal with a consequent reduction of entropy.

VI. Conclusion

The novel metric proposed in this article employs the Von Neumann entropy concept introduced in quantum information theory. Since the received GNSS-R signal is treated as a quantum state, it can be associated with a pure state when characterized by the presence of only one strong coherent component or to a mixed state in the case of incoherent components. In order to provide a suitable criterion for investigating the coherence of GNSS-R signals (which is equivalent to distinguishing a pure state from a mixed one), the received coherent signal is modeled as the superposition of a discrete, finite number of components. Thus, the density matrix formalism was applied to the correlation matrix of the received complex zero-Doppler delay waveforms. Indeed, it turns out that entropy is a powerful tool, expressing very effectively the dynamic range between the eigenvalues associated with the coherently scattered component and the other eigenvalues.

A first validation of the entropy-based coherence metric was provided by comparing results obtained on CYGNSS

data over Lake Okeechobee with Sentinel-1 images. Upon visual inspection, the sensitivity of entropy to forward scatter over water and wetlands is evident. In the presence of a strong coherent component, the entropy ranges from 0.18 to 0.4, such as on calm lake waters or on areas with floating vegetation. In contrast, entropy ranges from 0.75 to 0.9 when the incoherent component dominates, such as over rough lake waters or densely vegetated areas. In the wake of this initial analysis, it is worth investigating further the ability to discriminate among different types of vegetation coverage.

Furthermore, the metric can be implemented onboard GNSS-R receivers in space, in order to dynamically change the incoherent integration time, depending on the degree of coherence detected in real-time, thus achieving a marked improvement in spatial resolution. In this perspective, numerical calculation of entropy could be expensive. Nevertheless, there are several techniques that allow entropy to be computed efficiently and with a low memory occupancy.

ACKNOWLEDGMENT

The authors would like to thank Prof. Christopher Ruf from the University of Michigan and the CYGNSS team for providing the CYGNSS L0 raw data and making the L1 data publicly available through the NASA EOSDIS Physical Oceanography Distributed Active Archive Center (PO.DAAC). They would also like to thank Dr. Valery Zavorotny and the Wetlands Team of NNH17ZDA001N for useful discussions during the preparation of the manuscript. The research reported here was carried out in part at the Jet Propulsion Laboratory, Caltech.

REFERENCES

[1] M. Martín-Neira, "A passive reflectometry and interferometry system (PARIS): Application to ocean altimetry," *ESA J.*, vol. 17, no. 4, pp. 331–355, 1993.

[2] A. Komjathy, V. U. Zavorotny, P. G. Axelrad, G. H. Born, and J. L. Garrison, "GPS signal scattering from sea surface: Wind speed retrieval using experimental data and theoretical model," *Remote Sens. Environ.*, vol. 73, no. 2, pp. 162–174, Aug. 2000.

[3] S. Gleason, "Space-based GNSS scatterometry: Ocean wind sensing using an empirically calibrated model," *IEEE Trans. Geosci. Remote Sens.*, vol. 51, no. 9, pp. 4853–4863, Sep. 2013.

[4] M. Clarizia and C. S. Ruf, "Wind speed retrieval algorithm for the cyclone global navigation satellite system (CYGNSS) mission," *IEEE Trans. Geosci. Remote Sens.*, vol. 54, no. 8, pp. 4419–4432, Aug. 2016.

[5] A. Camps *et al.*, "Sensitivity of GNSS-R spaceborne observations to soil moisture and vegetation," *IEEE J. Sel. Topics Appl. Earth Observ. Remote Sens.*, vol. 9, no. 10, pp. 4730–4742, Oct. 2016.

[6] C. Chew, R. Shah, C. Zuffada, G. Hajj, D. Masters, and A. J. Mannucci, "Demonstrating soil moisture remote sensing with observations from the UK TechDemoSat-1 satellite mission," *Geophys. Res. Lett.*, vol. 43, no. 7, pp. 3317–3324, 2016.

[7] S. V. Nghiem *et al.*, "Wetland monitoring with global navigation satellite system reflectometry," *Earth Space Sci.*, vol. 4, no. 1, pp. 16–39, 2017.

[8] S. Gleason, "Towards sea ice remote sensing with space detected GPS signals: Demonstration of technical feasibility and initial consistency check using low resolution sea ice information," *Remote Sens.*, vol. 2, no. 8, pp. 2017–2039, Aug. 2010.

[9] H. Carreno-Luengo and A. Camps, "First dual-band multiconstellation GNSS-R scatterometry experiment over boreal forests from a stratospheric balloon," *IEEE J. Sel. Topics Appl. Earth Observ. Remote Sens.*, vol. 9, no. 2, pp. 4743–4751, Oct. 2016.

[10] H. Carreno-Luengo, A. Camps, J. Querol, and G. Forte, "First results of a GNSS-R experiment from a stratospheric balloon over boreal forests," *IEEE Trans. Geosci. Remote Sens.*, vol. 54, no. 5, pp. 2652–2663, May 2016.

[11] C. Chew *et al.*, "SMAP radar receiver measures land surface freeze/thaw state through capture of forward-scattered L-band signals," *Remote Sens. Environ.*, vol. 198, pp. 333–344, Sep. 2017.

[12] H. Carreno-Luengo, S. Lowe, C. Zuffada, S. Esterhuizen, and S. Oveisgharan, "Spaceborne GNSS-R from the SMAP mission: First assessment of polarimetric scatterometry over land and cryosphere," *Remote Sens.*, vol. 9, no. 4, p. 362, Apr. 2017.

[13] A. Alonso-Arroyo, V. U. Zavorotny, and A. Camps, "Sea ice detection using UK TDS-1 GNSS-R data," *IEEE Trans. Geosci. Remote Sens.*, vol. 55, no. 9, pp. 4989–5001, Sep. 2017.

[14] W. Li, E. Cardellach, F. Fabra, A. Rius, S. Ribó, and M. Martín-Neira, "First spaceborne phase altimetry over sea ice using TechDemoSat-1 GNSS-R signals," *Geophys. Res. Lett.*, vol. 44, pp. 8369–8376, Aug. 2017.

[15] C. Chew, A. Colliander, R. Shah, C. Zuffada, and M. Burgin, "The sensitivity of ground-reflected GNSS signals to near-surface soil moisture, as recorded by spaceborne receivers," in *Proc. Int. Geosci. Remote Sens. Symp. (IGARSS)*, Jul. 2017, pp. 2661–2663.

[16] C. S. Ruf *et al.*, "A new paradigm in earth environmental monitoring with the CYGNSS small satellite constellation," *Sci. Rep.*, vol. 8, no. 1, p. 8782, 2018.

[17] C. Gerlein-Safdi and C. S. Ruf, "A CYGNSS-based algorithm for the detection of inland waterbodies," *Geophys. Res. Lett.*, vol. 46, no. 21, pp. 12065–12072, 2019.

[18] M. Morris, C. Chew, J. T. Reager, R. Shah, and C. Zuffada, "A novel approach to monitoring wetland dynamics using CYGNSS: Everglades case study," *Remote Sens. Environ.*, vol. 233, Nov. 2019, Art. no. 111417.

[19] N. Rodriguez-Alvarez, E. Podest, K. Jensen, and K. C. McDonald, "Classifying inundation in a tropical wetlands complex with GNSS-R," *Remote Sens.*, vol. 11, no. 9, p. 1053, May 2019.

[20] J. Strandberg, T. Hobiger, and R. Haas, "Coastal sea ice detection using ground-based GNSS-R," *IEEE Geosci. Remote Sens. Lett.*, vol. 14, no. 9, pp. 1552–1556, Jul. 2017.

[21] C. Chew, C. Zuffada, R. Shah, and A. Mannucci, "Mapping sea ice using reflected GNSS signals in a bistatic radar system," in *Proc. EGU Gen. Assem. Conf. Abstr.*, Apr. 2016, p. 1.

[22] N. Rodriguez-Alvarez, B. Holt, S. Jaruwatanadilok, E. Podest, and K. C. Cavanaugh, "An Arctic sea ice multi-step classification based on GNSS-R data from the TDS-1 mission," *Remote Sens. Environ.*, vol. 230, Sep. 2019, Art. no. 111202.

[23] J. Cartwright, C. Banks, and M. Srokosz, "Sea ice detection using GNSS-R data from TechDemoSat-1," *J. Geophys. Res., Oceans*, vol. 124, no. 8, pp. 5801–5810, 2019.

[24] M. M. Al-Khaldi, J. T. Johnson, S. Gleason, E. Loria, A. J. O'Brien, and Y. Yi, "An algorithm for detecting coherence in Cyclone global navigation satellite system mission level-1 delay-Doppler maps," *IEEE Trans. Geosci. Remote Sens.*, vol. 59, no. 5, pp. 4454–4463, May 2021.

[25] E. Loria, A. O'Brien, and I. J. Gupta, "Detection & separation of coherent reflections in GNSS-R measurements using CYGNSS data," in *Proc. IEEE Int. Geosci. Remote Sens. Symp. (IGARSS)*, Jul. 2018, pp. 3995–3998.

[26] C. Roesler, Y. Wang, Y. J. Morton, and R. S. Nerem, "Coherent GPS reflections over ocean surface," in *Proc. IEEE Int. Geosci. Remote Sens. Symp. (IGARSS)*, Sep. 2020, pp. 6218–6221.

[27] I. M. Russo, M. di Bisceglie, C. Galdi, M. Lavalle, and C. Zuffada, "Wave coherence in GNSS reflectometry: A signal processing point of view," in *Proc. IEEE Int. Geosci. Remote Sens. Symp. (IGARSS)*, Sep. 2020, pp. 6214–6217.

[28] A. G. Voronovich and V. U. Zavorotny, "Bistatic radar equation for signals of opportunity revisited," *IEEE Trans. Geosci. Remote Sens.*, vol. 56, no. 4, pp. 1959–1968, Apr. 2018.

[29] F. T. Ulaby, R. K. Moore, and A. K. Fung, *Microwave Remote Sensing: Active and Passive, Artech House Remote Sensing Library*. Norwood, MA, USA: Artech House, 1986.

[30] H. Carreno-Luengo, G. Luzi, and M. Crosetto, "First evaluation of topography on GNSS-R: An empirical study based on a digital elevation model," *Remote Sens.*, vol. 11, no. 21, p. 2556, Oct. 2019.

[31] J. D. Campbell, A. Melebari, and M. Moghaddam, "Modeling the effects of topography on delay-Doppler maps," *IEEE J. Sel. Topics Appl. Earth Observ. Remote Sens.*, vol. 13, pp. 1740–1751, 2020.

[32] F. Martin *et al.*, "Mitigation of direct signal cross-talk and study of the coherent component in GNSS-R," *IEEE Geosci. Remote Sens. Lett.*, vol. 12, no. 2, pp. 279–283, Feb. 2015.

[33] P. Beckmann and A. Spizzichino, *The Scattering of Electromagnetic Waves From Rough Surfaces*. New York, NY, USA: Pergamon Press, 1963.

[34] A. M. Balakhder, M. M. Al-Khaldi, and J. T. Johnson, "On the coherency of ocean and land surface specular scattering for GNSS-R and signals of opportunity systems," *IEEE Trans. Geosci. Remote Sens.*, vol. 57, no. 12, pp. 10426–10436, Dec. 2019.

[35] A. Egido *et al.*, "Airborne GNSS-R polarimetric measurements for soil moisture and above-ground biomass estimation," *IEEE J. Sel. Topics Appl. Earth Observ. Remote Sens.*, vol. 7, no. 5, pp. 1522–1532, May 2014.

[36] E. Loria, A. O'Brien, V. Zavorotny, and C. Zuffada, "Towards wind vector and wave height retrievals over inland waters using CYGNSS," *Earth Space Sci.*, vol. 8, no. 7, pp. 1–20, Jul. 2021.

[37] D. Comite, F. Ticconi, L. Dente, L. Guerriero, and N. Pierdicca, "Bistatic coherent scattering from rough soils with application to GNSS reflectometry," *IEEE Trans. Geosci. Remote Sens.*, vol. 58, no. 1, pp. 612–625, Jan. 2020.

[38] E. Loria, A. O'Brien, V. Zavorotny, B. Downs, and C. Zuffada, "Analysis of scattering characteristics from inland bodies of water observed by CYGNSS," *Remote Sens. Environ.*, vol. 245, Aug. 2020, Art. no. 111825.

[39] A. Fung and H. Eom, "Coherent scattering of a spherical wave from an irregular surface," *IEEE Trans. Antennas Propag.*, vol. AP-31, no. 1, pp. 68–72, Jan. 1983.

[40] F. T. Ulaby *et al.*, *Microwave Radar and Radiometric Remote Sensing*. Ann Arbor, MI, USA: Univ. Michigan Press, 2014.

[41] A. G. Voronovich and V. U. Zavorotny, "The transition from weak to strong diffuse radar bistatic scattering from rough ocean surface," *IEEE Trans. Antennas Propag.*, vol. 65, no. 11, pp. 6029–6034, Nov. 2017.

[42] P. Ferrazzoli, L. Guerriero, N. Pierdicca, and R. Rahmoune, "Forest biomass monitoring with GNSS-R: Theoretical simulations," *Adv. Space Res.*, vol. 47, no. 10, pp. 1823–1832, 2010.

[43] L. Guerriero, N. Pierdicca, L. Pulvirenti, and P. Ferrazzoli, "Use of satellite radar bistatic measurements for crop monitoring: A simulation study on corn fields," *Remote Sens.*, vol. 5, no. 2, pp. 864–890, 2013.

[44] V. U. Zavorotny and A. G. Voronovich, "Scattering of GPS signals from the ocean with wind remote sensing application," *IEEE Trans. Geosci. Remote Sens.*, vol. 38, no. 2, pp. 951–964, Mar. 2000.

[45] A. Camps, "Spatial resolution in GNSS-R under coherent scattering," *IEEE Geosci. Remote Sens. Lett.*, vol. 17, no. 1, pp. 32–36, Jan. 2020.

[46] A. Camps and J. F. Munoz-Martin, "Analytical computation of the spatial resolution in GNSS-R and experimental validation at L1 and L5," *Remote Sens.*, vol. 12, no. 23, p. 3910, Nov. 2020.

[47] J. B.-Y. Tsui, *Fundamentals of Global Positioning System Receivers: A Software Approach*, Hoboken, NJ, USA: Wiley, 2000.

[48] F. Bouchereau, D. Brady, and C. Lanzl, "Multipath delay estimation using a superresolution PN-correlation method," *IEEE Trans. Signal Process.*, vol. 49, no. 5, pp. 938–949, May 2001.

[49] T. Manabe and H. Takai, "Superresolution of multipath delay profiles measured by PN correlation method," *IEEE Trans. Antennas Propag.*, vol. 40, no. 5, pp. 500–509, May 1992.

[50] R. O. Schmidt, "Multiple emitter location and signal parameter estimation," *IEEE Trans. Antennas Propag.*, vol. AP-34, no. 3, pp. 276–280, Mar. 1986.

[51] F. Martin, S. D'Addio, A. Camps, and M. Martin-Neira, "Modeling and analysis of GNSS-R waveforms sample-to-sample correlation," *IEEE J. Sel. Topics Appl. Earth Observ. Remote Sens.*, vol. 7, no. 5, pp. 1545–1559, May 2014.

[52] D. Bicout and C. Brosseau, "Multiply scattered waves through a spatially random medium: Entropy production and depolarization," *J. Phys.*, vol. 2, pp. 2047–2063, Nov. 1992.

[53] M. C. Harwell and B. Sharfstein, "Submerged aquatic vegetation and bulrush in lake Okeechobee as indicators of greater Everglades ecosystem restoration," *Ecol. Indicators*, vol. 9, no. 6, pp. S46–S55, Nov. 2009.

[54] C. Ruf *et al.*, *CYGNSS Handbook*. Racine, WI, USA: Michigan Pub, 2016.

[55] *National Wetlands Inventory Website*, U.S. Dept. Interior, Washington, DC, USA, Oct. 2020. [Online]. Available: http://www.fws.gov/wetlands/

[56] *Classification Wetlands Deepwater Habitats United States, FGDC-STD-004-2013*, U.S. Fish Wildlife Service, Washington, DC, USA, 2013.

[57] K. E. Havens and D. E. Gawlik, "Lake Okeechobee conceptual ecological model," *Wetlands*, vol. 25, no. 4, pp. 908–925, Dec. 2005.

Ilaria Mara Russo (Member, IEEE) received the bachelor's and master's degrees *(summa cum laude)* in electronic engineering for automation and telecommunication from the Università degli Studi del Sannio, Benevento, Italy, in 2015 and 2018, respectively, where she is currently pursuing the Ph.D. degree in information technologies for engineering.

In 2020, she was a Visiting Research Student at the Jet Propulsion Laboratory (JPL), California Institute of Technology, Pasadena, CA, USA. Her research interest includes global navigation satellite system (GNSS) signal processing techniques for remote sensing using GNSS reflectometry.

Maurizio di Bisceglie (Member, IEEE) was born in Naples, Italy. He received the Laurea degree in electronic engineering and the Ph.D. degree in electronic and information systems engineering from the Università degli Studi di Napoli Federico II, Naples, Italy, in 1988 and 1993, respectively.

Since 1998, he has been with the Università degli Studi del Sannio, Benevento, Italy, as an Associate Professor of telecommunications. He was a Visiting Scientist at University College London, London, U.K., and the Defense Evaluation and Research Agency, Malvern, U.K. His scientific activities include participation in the Organizing Committee of the Italian phase of the European AQUA Thermodynamic Experiment (EAQUATE) mission in 2004, organization of the NASA Direct Readout Conference in 2005, and participation in the Organizing Committee of the IEEE 2008 Radar Conference. During the last ten years, he has been involved in global navigation satellite system (GNSS) reflectometry in collaboration with several institutions, including the National Oceanography Center from 2007 to 2012, the University of Michigan (CYGNSS Science Team since 2015), and the Jet Propulsion Laboratory (Wetlands Team since 2019). His research interests are in the field of signal processing and stochastic modeling in remote sensing.

Dr. Di Bisceglie was the Chair of the IEEE GNSS+R Meeting in 2019. He is a permanent member of the GNSS+R Conference Steering Committee.

Carmela Galdi (Member, IEEE) received the Dr.Eng. and Ph.D. degrees in electronic engineering from the Università degli Studi di Napoli Federico II, Naples, Italy, in 1992 and 1997, respectively.

In 1995, she was at the Signal Processing Division, University of Strathclyde, Glasgow, U.K., with an Erasmus Fellowship. In 1997, she was a Visiting Scientist at University College London, London, U.K., and the Defense Evaluation and Research Agency, Malvern, U.K, working on statistical models of radar backscattering from natural surfaces. From 1997 to 2000, she was a Post-Doctoral Researcher at the Università degli Studi di Napoli Federico II. In 2000, she joined the Università degli Studi del Sannio, Benevento, Italy, where she is currently an Associate Professor of telecommunications. She has cooperated with the National Oceanography Centre (NOC), Southampton, U.K., on a project about global navigation satellite system reflectometry (GNSS-R) of the ocean surface. She is associated with the NASA CYGNSS project as an external science team member, working on the development of science algorithms for GNSS-R. Her research interests are in the fields of statistical signal processing, non-Gaussian models of radar backscattering, and global navigation satellite system reflectometry.

Dr. Galdi served on the Organizing Committee of the IEEE 2008 Radar Conference. She was the Co-Chair of the IEEE 2019 GNSS+R Specialist Meeting.

Marco Lavalle (Member, IEEE) received the M.Sc. degree in telecommunication engineering from the University of Rome Tor Vergata, Rome, Italy, in 2006, and the Ph.D. degree from the University of Rennes 1, Rennes, France, and the University of Rome Tor Vergata in December 2009.

From 2006 to 2008, he was Visiting Scientist at the European Space Agency (ESRIN), Frascati, Italy, where he supported ESA's activities on polarimetric radar calibration and polarimetric radar interferometry science-algorithm development. From January 2010 to December 2011, he was a NASA Post-Doctoral Fellow at the Jet Propulsion Laboratory (JPL), California Institute of Technology, Pasadena, CA, USA. He is currently a Scientist with the NASA Jet Propulsion Laboratory, California Institute of Technology. He has been a permanent Scientist at the Radar Science and Engineering Section, JPL, since January 2012. He has been a Principal Investigator and a Co-Investigator for several NASA programs. He is the lead for the 2020 NASA Distributed Aperture Radar Tomographic Sensors (DARTS) Project and a member of the ESA ROSE-L, NASA CYGNSS, and JPL NISAR and UAVSAR Project Science Teams. His research interests include retrieval algorithm development, physical and statistical model formulation, electromagnetic propagation, scattering theory, synthetic aperture radar (SAR) tomography, polarimetric SAR interferometry, ecosystem modeling, and surface parameter estimation.

Dr. Lavalle was a recipient of the 2019 NASA Early Career Public Achievement Medal, the 2020 JPL Lew Allen Award for Excellence, and the Student Prize Paper Award at the EUSAR 2008 Conference, Friedrichshafen, Germany.

Cinzia Zuffada (Senior Member, IEEE) received the Doctorate of Engineering degree from the University of Pavia, Pavia, Italy, in 1979.

She joined NASA's Jet Propulsion Laboratory, Pasadena, CA, USA, in 1992, where she is currently an Associate Chief Scientist. As such, she is a key contributor to the strategic planning of science and technology research and development directions for JPL and to managing institutional internal research and development investments. In addition, she oversees a number of programs supporting collaborations between JPL and the academic community. Since the late 1990s, she has led some pioneering GNSS reflectometry technology development awarded through the NASA IIP and has played a pivotal role in demonstrating the feasibility of the GPS altimetry measurement from fixed sites and airplanes. More recently, she has been focusing on the application of GNSS Reflectometry to detect surface water, as a member of the competed science team of NASA CYGNSS. She has been a member of the Science Advisory Group for GEROS. She was a tenured Researcher in electromagnetic field (EM) theory with the University of Pavia before moving to USA, where she worked in EM scattering and radiation problems.

Dr. Zuffada is a member of URSI Commission B and American Geophysical Union (AGU). She received the Teresian Medal from the University of Pavia in 2002, the Magellan Award from JPL in 2014, the Outstanding Leadership Award from NASA in 2015, and the Knighthood of Order of Merit of the Italian Republic in 2015. She is an Associate Editor of TGARS. She is also a member of the Science Advisory Group for HydroGNSS, two ESA GNSS reflectometry experiments.